Study on Weldability and Mechanical Properties of RSW Annular-Nugget Joint. Part 1 — FEM and Characterization Results

The advantages of the new ring conductive electrode over the conventional spherical electrode for DP780 steel were investigated

BY S. WANG, G. XU, J. DONG, Y. QIU, Q. FAN, Z. HUANG, AND X. GU

Abstract

The weldability of DP780 steel using resistance spot welding (RSW) was studied by comparing a new ring conductive electrode (RSW-R) and a spherical electrode (RSW-S). The mechanism of the RSW process of annular-nugget on the weldability was analyzed by examining the joint's current density and thermal field. Finite element analysis revealed that under RSW-R conditions, the annular conductive area expanded the contact area of the faying surface and reduced the nugget's current density. This characteristic effectively mitigated the risk of expulsion associated with high heat input rates and excessively high liquid metal temperatures while enhancing energy utilization. Mechanical property tests demonstrated that variations in heat input efficiency during nugget growth affected the weldability range, with the annular-nugget joints achieving a 1.5-fold increase in range compared to RSW-S. In addition, when using RSW-R, a larger nugget diameter was achieved with less Joule heating. The maximum nugget diameter increased by 17.38%, and the indentation depth was significantly reduced by 48.65% compared to RSW-S.

Keywords

- Resistance Spot Welding
- DP780 Steels
- Annular-Nugget
- Finite Element
- Weldability
- Current Density
- Thermal Field
- Indentation Depth

https://doi.org/10.29391/2025.104.014

Introduction

The transportation industry faces significant challenges due to the growing energy crisis and environmental pollution (Refs. 1, 2). Aluminum alloy has become a popular choice for automotive lightweighting. However, their limitations in strength and weldability restrict their use in critical structures such as the body-in-white (Ref. 3). Dual-phase steels, a type of advanced high-strength steels (AHSS), comprise a ferrite matrix with martensite as the second phase. The balance of strength and ductility makes dual-phase steels highly favored by automotive manufacturers (Ref. 4). Their high strength-to-mass ratio maintains structural integrity while allowing for reduced sheet thickness and vehicle weight.

Resistance spot welding (RSW) is one of the most widely used welding technologies in the automotive industry due to its characteristics of being easily automated, high efficiency, low cost, and operational flexibility (Refs. 5–7). However, the high alloy content in AHSS can lead to an increase in resistivity, which in turn raises the heat input during welding. This can cause expulsion and limit the upper weldability threshold (Ref. 8). Additionally, the high alloy content promotes the formation of shrinkage cavities, reduces the interfacial bearing area, and leads to interfacial fracture (Ref. 9).

Several researchers have conducted studies to address these challenges. Ling et al. proposed a new resistance spot welding method for double-sided cover sheets, which effectively increased the contact area between sheets, reduced the current density during welding, delayed expulsion, and improved the weldability of galvanized ultra-high-strength steels (Ref. 10). Gerardo et al. found that inverter frequency significantly impacts weld quality, with high-frequency

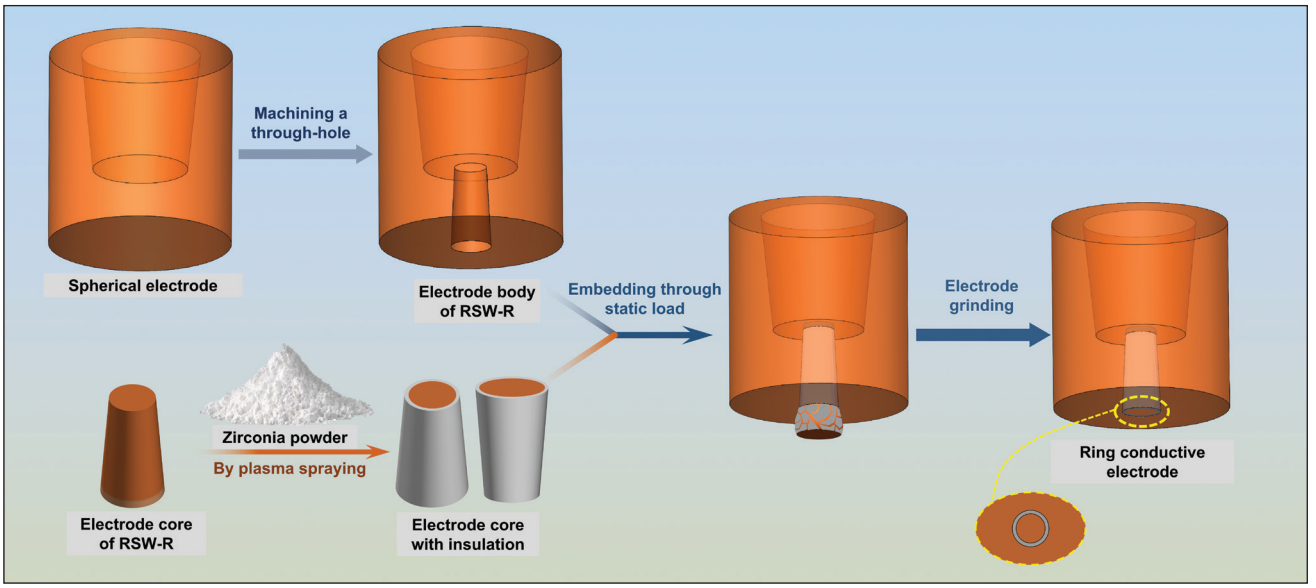

Fig. 1 — Schematic diagram of the fabrication process of ring conductive electrodes.

Table 1 — Mechanical Properties and Chemical Compositions of DP780 Steel

Steel	Chemical Composition (wt-%)						Mechanical Properties		
	C	Mn	Al	Si	P	S	YS (MPa)	UTS(MPa)	EL(%)
DP780	0.086	2.11	0.038	0.193	0.011	0.001	452	817	19.5

inverters providing a wider weldability lobe (Ref. 11). Díaz et al. improved the weldability of advanced high-strength steels (Q&P-AHSS) through short-term annealing and isothermal treatments (Ref. 12). Xu developed small inserts for welding different micro-alloyed and dual-phase steels using the projection welding method (Ref. 13). Li et al. combined current pulse technology with magnetically assisted resistance spot welding to significantly increase nugget size, refine grain size, and expand the weldability range of press-hardened steels (Ref. 3). These studies have made notable contributions to improving RSW joint weldability. However, it is undeniable that the additional steps proposed in these studies reduce production efficiency.

To retain production efficiency while enhancing the RSW weldability of AHSS, several studies have focused on changing the heat input distribution in RSW by modifying the electrode design. Chen et al. designed a micro concave electrode to optimize current density distribution and significantly improve the weldability of Q&P steels (Ref. 14). Watanabe et al. (Ref. 15) used a concave electrode with a deep hole to expand the welding current range of DP980 steels. However, these surface modifications can create grooves or protrusions on the joint surface, resulting in poor surface quality and stress concentration that degrade mechanical properties. Ren et al. achieved annular current distribution by embedding insulating ceramic in the electrode, resulting in joints with smaller indentation depths, larger nugget areas, and wider welding process windows (Refs. 16–18). However, significant differences in thermal properties, such as thermal conductivity and thermal expansion coefficient between insulating ceramics and copper alloy electrodes, may adversely affect electrode heat dissipation efficiency and service life.

This study introduces a new ring conductive electrode (RSW-R) designed to enhance the weldability of DP780 steel RSW joints by modifying the current distribution of F-type electrodes (RSW-S). Numerical simulations were conducted to analyze the variations in current density and thermal fields between the two types of electrodes, and the factors contributing to improved weldability under RSW-R conditions were identified. The findings provided more profound insights into the growth mechanism of annular-nuggets and their role in enhancing the weldability of RSW joints.

Experimental Details

Electrode Cap for RSW

In this study, a new ring conductive electrode (RSW-R) and a standard spherical electrode (RSW-S, AWS C1.1M/C1.1:2012, *Recommended Practices for Resistance Welding*) (Ref. 19)

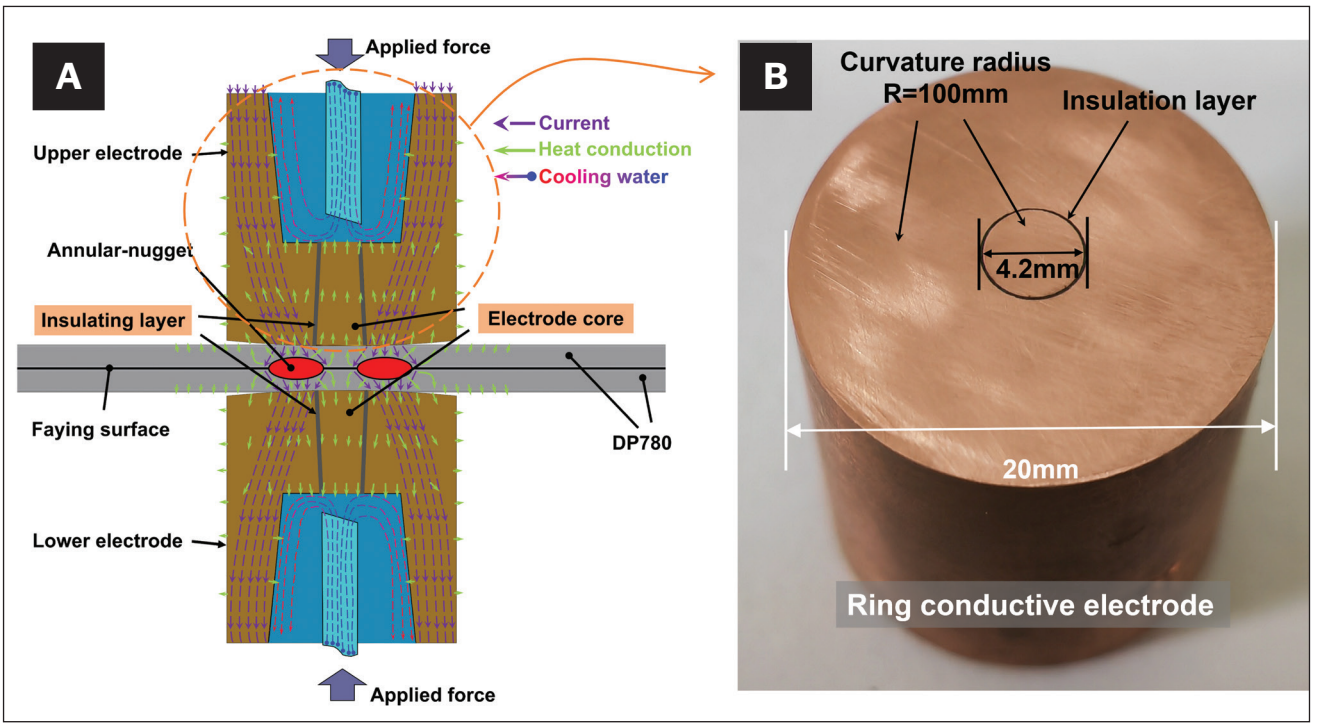

Fig. 2 — A — RSW joint model under ring conductive electrode; B — ring conductive electrode.

were selected for experimentation. Both types of electrodes were fabricated from the same Cu-Cr-Zr alloy (RWMA class 2, C18150) (Ref. 20). The manufacturing process of the RSW-R is illustrated in Fig. 1. The RSW-R was created by machining a circular truncated conical through-hole in the core of the RSW-S, followed by embedding an electrode core into the hole. The surface of the electrode was then ground to a curvature radius of 100 mm. To minimize differences in physical properties such as thermal conductivity and coefficient of thermal expansion between the electrode body and the electrode core, both components were made from C18150. Insulation was achieved by plasma spraying a 50-µm layer of zirconia onto the side of the electrode core. Figure 2A provides a schematic of the welded joint under the RSW-R conditions, showing the relative positions of the electrode core and insulating layer. Figure 2B presents a photograph of the RSW-R and its relevant dimensions.

Material and Welding Process

A 1.2 mm thick DP780 steel sheet was selected as the base material (BM) for this study. The mechanical properties of the steel sheet are provided in Table 1. As shown in Fig. 3, the RSW test samples were produced using a welding setup consisting of a medium-frequency transformer (Rexroth PSG 6130), a medium-frequency inverter (Rexroth PSI 63C0), and a servo press (IAI SCON-CB). The welding was conducted on a custom-designed punch welding frame. Before welding, electrode alignment is achieved by adjusting the screws on the lower electrode base to ensure the lower electrode axis coincides with the upper electrode axis. Welding parameters were set via a computer, with the servo press and welding controller linked by a programmable logic controller (PLC). Dynamic signals from the welding process were recorded using external current (Meatrol Rogowski) and voltage sensors (Ref. 21), with a signal acquisition frequency of 10kHz. A plot of the current-voltage product over time was generated by multiplying the 2000 welding current values during the 0.2 s welding period by the corresponding voltage values at each moment. Joule heat input was calculated from the area between this curve and the x-axis. Welding parameters such as current, electrode force, and welding time are listed in Table 2. Each welding parameter was tested with at least three samples, with a minimum interval of one minute between welds.

Mechanical Test and Metallographic Observation

The welded specimens were subjected to uniaxial tensile-shear testing (MTS810) following the ANSI/AWS/SAE/D8.9, *Recommended Practices for Test Methods for Evaluating the Resistance Spot Welding Behavior of Automotive Sheet Steel Materials* standard (Ref. 22). Joint indentation was measured using a 3D optical surface profiler (New View 9000). RSW joints were cross-sectioned from the center using a wire-cut electrical discharge machining (WEDM) to prepare metallographic samples. The samples were mounted in epoxy resin, polished following standard procedures, and chemically etched with 2% Nital solution (Ref. 23). A Zeiss Scope A1 digital optical microscope was used to capture images of these samples. The various regions of the annular-nugget joint cross section were defined as shown in Fig. 4. The inner diameter (RSW-R_{in}) and outer diameter (RSW-R_{out}) of the annular-nugget were determined based on previous work (Ref. 18).

Numerical Simulation

Due to the model's symmetry, a ¼ axisymmetric 3D solid model was chosen for numerical simulation to reduce computation time. The solid parts were imported into the ABAQUS pre-processing module for assembly. To improve solution efficiency while maintaining simulation accuracy, the mesh in the direct contact area between parts was refined using a nonuniform division method (Ref. 24). Q3D8R mesh cells were used to analyze current and temperature variations. The critical mechanical and physical properties of the materials were obtained from JMatPro. The boundary conditions and interface contact properties were taken from previous work (Ref. 25).

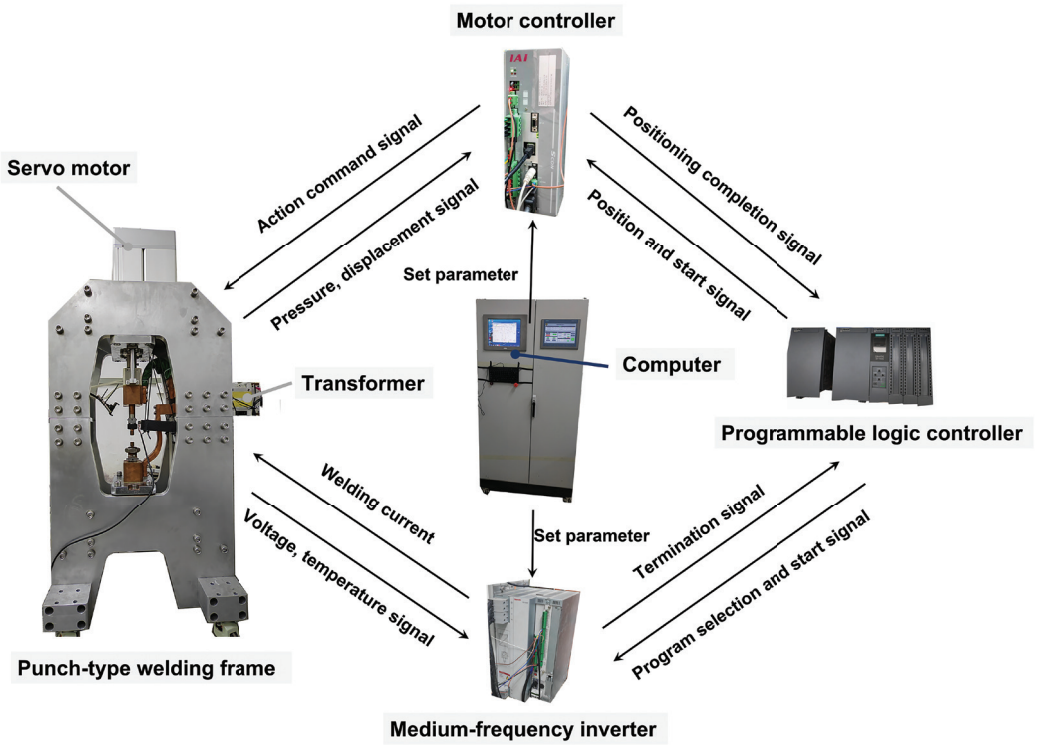

Fig. 3 — Schematic diagram of the RSW welding system.

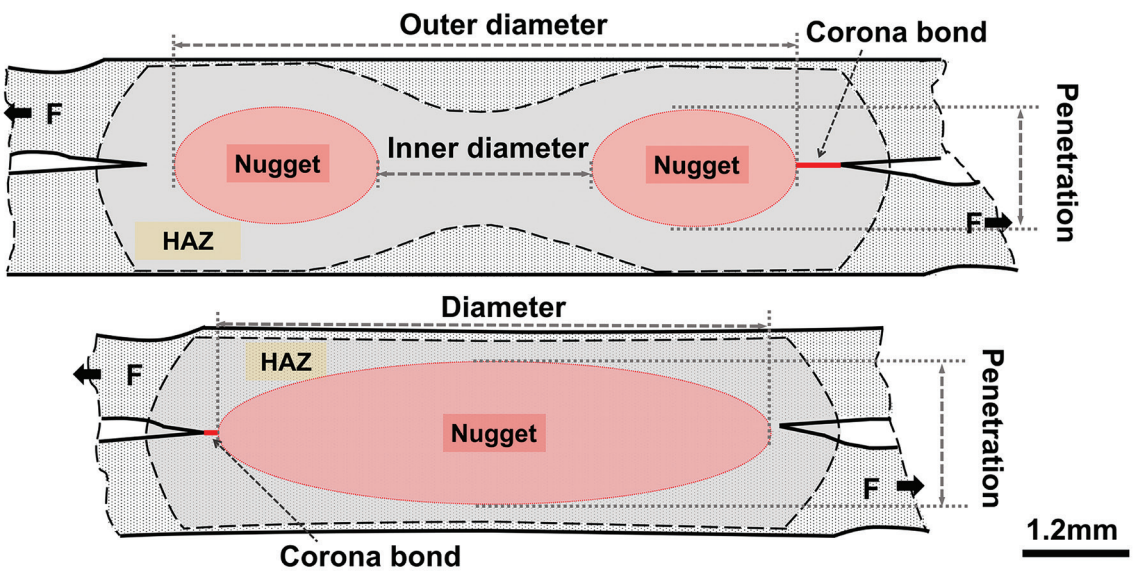

Fig. 4 — Schematic diagram of the various regions of the joint cross-section.

Results

Nugget Size and Weldability

As shown in Fig. 5, the microstructure of base metal (DP780 steel) consists of ferrite and martensite islands. Figure 6 compares the metallographic images of the joint cross sections for different welding currents under RSW-S and RSW-R conditions. Under identical welding parameters, the outer diameter of the RSW-R joints was consistently larger than that of the RSW-S joints, with the differences increasing as the current increased. However, the variation in nugget penetration between the two electrode types diminished as the current increased.

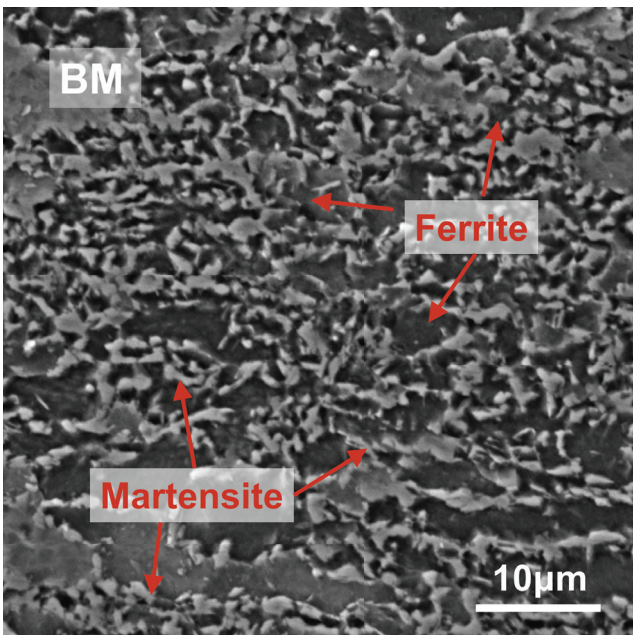

Fig. 5 — Microstructure of the DP780 steel base material.

Figure 7 illustrates the changes in outer diameter, inner diameter, and nugget area with increasing welding current. Under RSW-R conditions, the inner diameter of the annular-nugget decreased with increasing current until it disappeared, and the nugget became continuous. The maximum outer diameter of the nuggets before expulsion under RSW-R conditions was 8.24 mm, 17.38% larger than the 7.02 mm observed under RSW-S conditions. Similarly, the maximum nugget area before expulsion significantly increased by 30.32%. The current range from the onset of pullout fracture (PF) to the maximum current before expulsion was 9–11kA for RSW-S, while for RSW-R, it was 10–13kA, achieving a 1.5-fold increase in weldability range compared to RSW-S.

Joule Heat Input and Indentation

Figure 8 demonstrates that Joule heat inputs increased with the welding current. Under identical parameters, the Joule heat input in RSW-R conditions was consistently lower than in RSW-S conditions.

The 3D contour schematic of joint indentations, as shown in Fig. 9A, reveals that unlike under the RSW-S condition, annular indentations were observed in annular-nugget joints. The indentation depths in annular-nugget joints were significantly smaller than those in elliptical nugget joints. Figure 9B compares the variation in joint indentation depth with welding current for both electrode conditions. The results indicated that when the maximum welding current (13kA for RSW-R and 11kA for RSW-S) was applied, the indentation depth on the surface of joints under the RSW-S condition was approximately 164.65μm. In contrast, it was about 84.49μm under the RSW-R condition. This represented a 48.65% reduction in indentation depth for RSW-R compared to RSW-S.

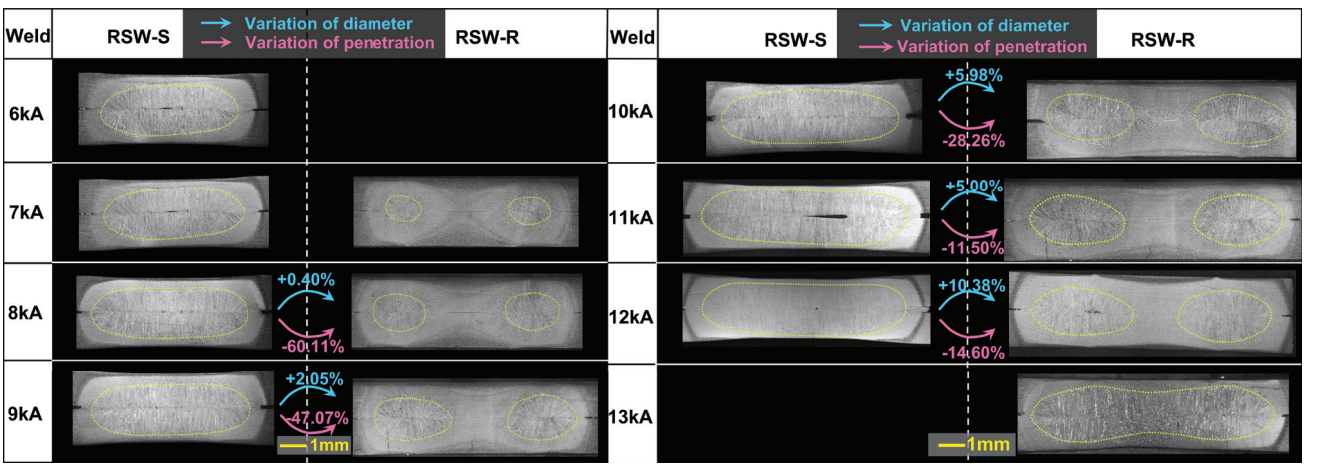

Fig. 6 — Metallographic diagram of the joint cross section under RSW-R and RSW-S conditions with a welding current of 6-13 kA.

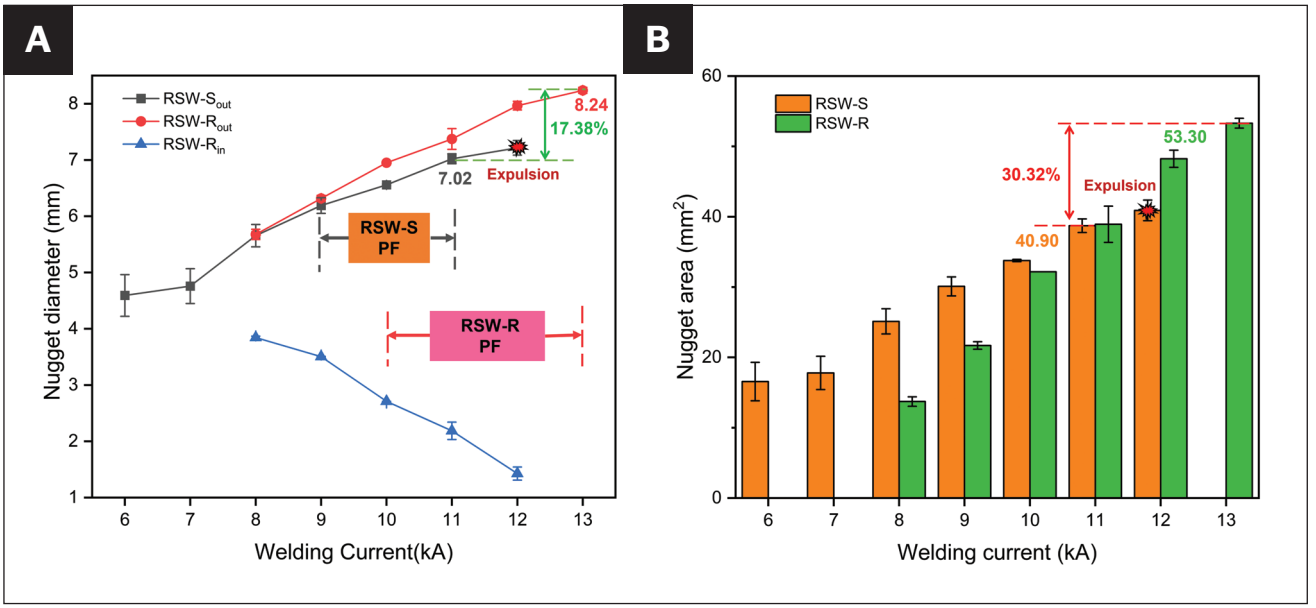

Fig. 7 — Variation of nugget size with welding current under RSW-R and RSW-S conditions by experiments: A — Inner and outer diameters of the nugget; B — nugget area.

Current Density Distribution and Thermal Field

Before conducting the analysis, the differences between the simulated and experimental results for the inner diameter, outer diameter, nugget penetration, and dynamic resistance signals of the nuggets under RSW-R and RSW-S conditions were compared. As shown in Fig. 10, the numerical simulation results closely matched the experimental measurements, confirming that the simulated thermal field and current density distribution from the finite element model were accurate (Ref. 21).

Since the contact area at the faying surface cannot be directly measured during welding, finite element analysis (FEM) was used to characterize the contact area changes throughout the welding process. In the finite element model, regions with a current density more significant than the minimum value of the current density contour (116.7×10^6 A/m^2) were considered the contact region. Figure 11 illustrates the contact area on the faying surface under two different electrode conditions. In Fig. 11A, the contact area under RSW-S conditions was concentrated only at the center of the joint, whereas in Fig. 11B, the contact area under RSW-R conditions not only covered the center of the joint but also included the annular region where between the annular conductive zone (ACZ). Additionally, point A in Fig. 11A represented the center of the nugget for RSW-S, while point B in Fig. 11B represented the center of the annular-nugget for RSW-R.

Figure 12 shows the simulated current density and temperature variations at the center of the nugget during welding. As illustrated in Fig. 12A, the current density at the nuggets' center under RSW-R conditions remained consistently lower than that under RSW-S conditions within the welding current range where pullout fracture (PF) occurs. Even with a welding current of 13kA for RSW-R, the current density was still lower than that under RSW-S conditions with a welding current of 9kA. The peak current density was reached quickly in all cases. Then, the current density decreased with increasing welding time for RSW-S at 9kA, RSW-S at 11kA, and RSW-R at 13kA.

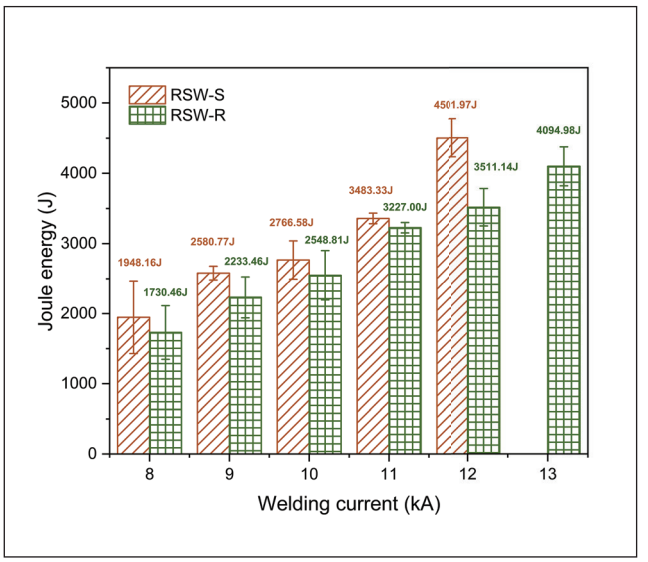

Fig. 8 — Variation of Joule heat input with welding current by experiments under RSW-R and RSW-S conditions.

In contrast, under RSW-R at 10kA, a plateau in current density was observed during the welding time of 0.015–0.085 s, followed by a significant increase in current density during the period of 0.085–0.11 s. As depicted in Fig. 12B, the nugget heating rate was slower under RSW-R conditions, resulting in a longer time to reach peak temperature than under RSW-S conditions. Furthermore, the dwell time above the melting point was shorter for RSW-R and RSW-S.

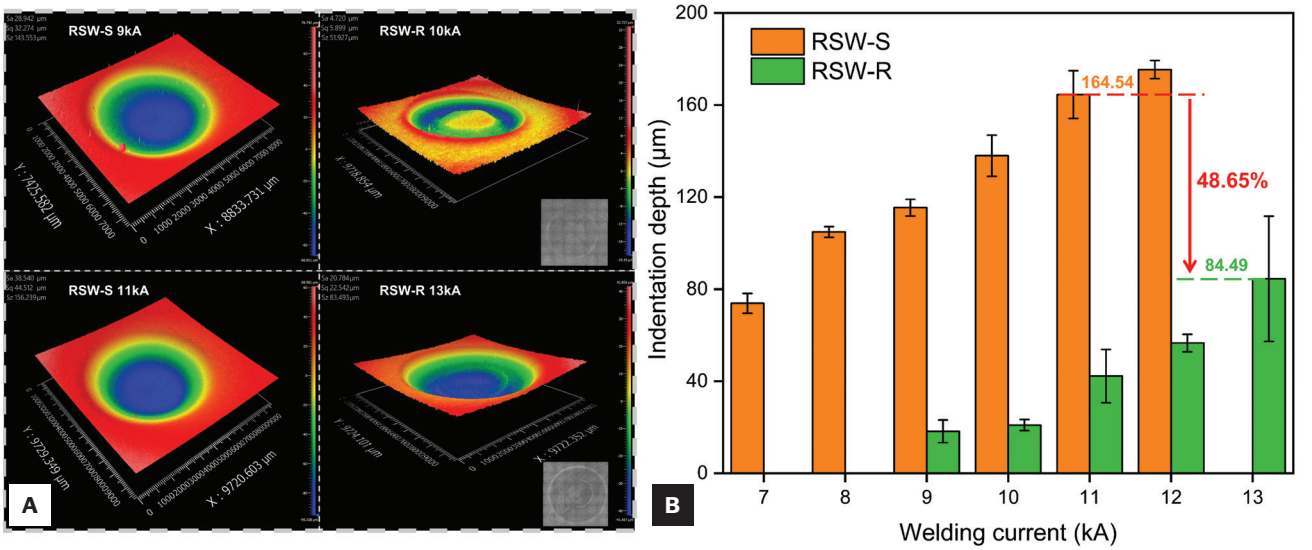

Fig. 9 — Variation of joint surface indentation with welding current under different electrode conditions: A — 3D contour of the joint surface; B — indentation depth on the joint surface by experiments.

Table 2 — Welding Parameters of the Welding Process

Electrode	Squeezing Time	Welding Time	Holding Time	Electrode Force	Welding Current
RSW-S	200 ms	200 ms	400 ms	4 kN	7–11 kA
RSW-R	200 ms	200 ms	400 ms	4 kN	8–13 kA

Discussion

Mechanism of Weldability Range Expansion

An increase in temperature from the melting point (Tm) to a specific temperature (T) causes a rise in pressure at constant volume (Ref. 26). Nugget growth is accompanied by pressure from the volume change during the transition from solid to liquid, as well as internal pressure caused by the thermal expansion of the liquid metal. The increase in these two pressures promotes expulsion, reduction in nugget size, deeper indentation, and deterioration of mechanical properties. Thus, minimizing internal pressure during the solid-to-liquid transition and reducing the thermal expansion of the liquid metal can effectively suppress expulsion and improve the weldability range of RSW. On the other hand, when the nugget size exceeds the corona bond size, expulsion will also occur (Ref. 27).

As shown in Fig. 12, within the weldability range, the current density under RSW-R conditions was generally lower than under RSW-S conditions. Additionally, the peak temperature of the nugget was typically lower with RSW-R than with RSW-S, and the duration above the melting point was also shorter under RSW-R conditions. Figure 8 demonstrates that, at the same welding current, the Joule heat input for RSW-R was consistently lower than for RSW-S. These differences in nugget temperature and Joule heat input between the two types of electrodes can be attributed to variations in nugget current density. Figure 12A shows that, before 0.11 s, the welding current density at the nugget center was generally higher under RSW-S than under RSW-R. The higher current density in RSW-S accelerated Joule heat generation, rapidly increasing the peak temperature of the liquid metal, while the more significant internal pressure from the expanding liquid metal promoted expulsion. Despite the significantly higher welding current applied to the RSW-R electrode, the current density at the nugget center remained consistently lower under RSW-R. This lower peak temperature and shorter duration above the melting point contributed to the expanded weldability range of RSW.

The optimization of joint current density with RSW-R was primarily attributed to the larger contact area at the faying surface. The total contact area influenced the average current density at the faying surface under different electrode conditions. Since the contact area cannot be directly measured during the welding process, factors such as surface roughness, changes in axial stress, and warping deformation of the sheets affect the contact area. Additionally, temperature variations during welding lead to fluctuations in current density across the faying surface. This study defined regions of the faying surface with current densities greater than 116.7 × 106 A/m^2 in the finite element model as contact areas.

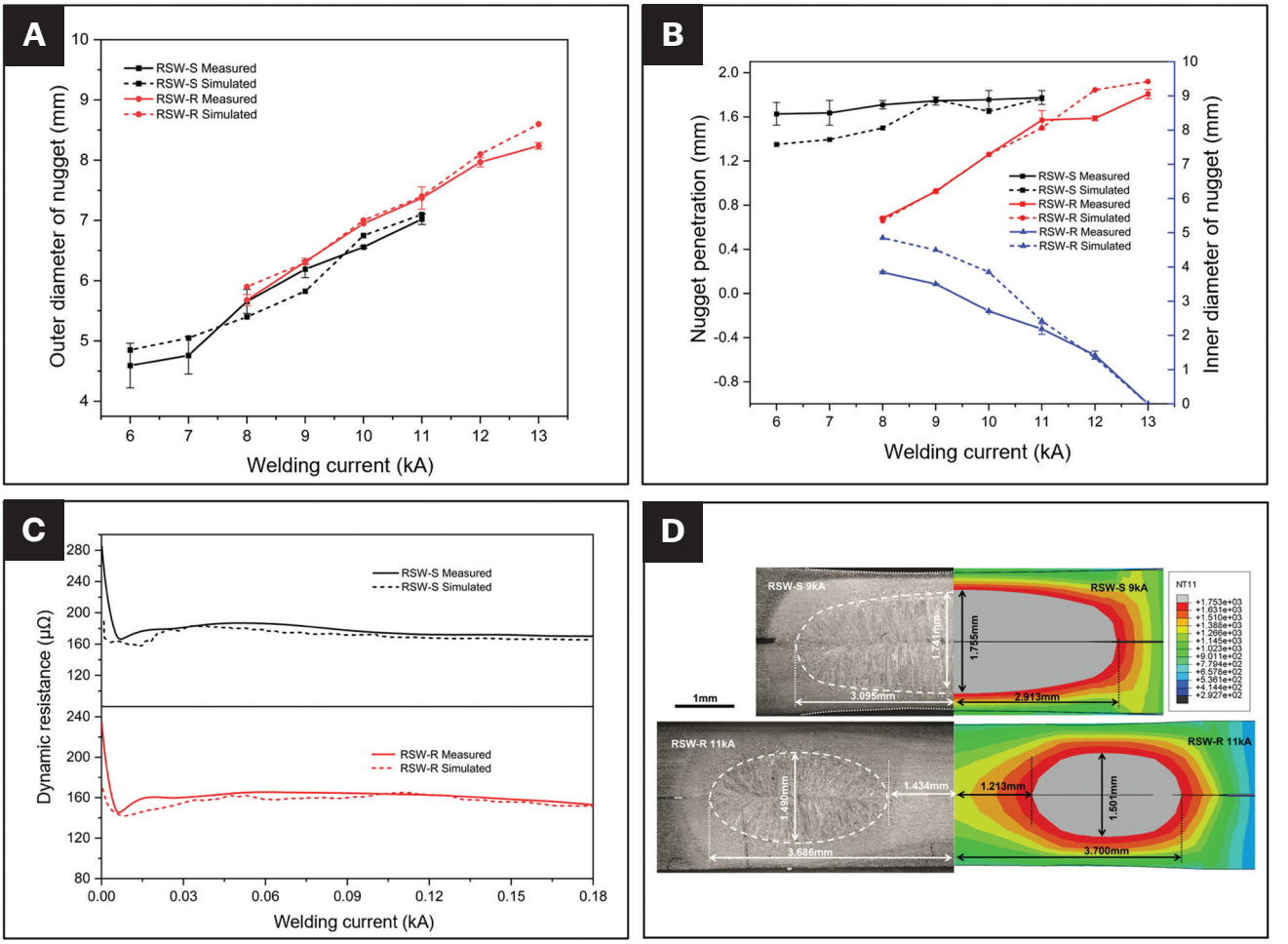

Fig. 10 — Comparison between simulated and measured results of RSW of DP780 steel under two types of electrode conditions: A — Outer diameter of nugget; B — inner diameter of nugget and nugget penetration; C — dynamic resistance; D — cross-section profile.

Figure 13 compares the current density distribution in joints under two types of electrode conditions at different time points, with the same welding current and maximum pullout fracture current. Regardless of the applied current, the contact area at the faying surface was significantly larger under RSW-R conditions than under RSW-S conditions during welding. This difference arises from the current flow characteristics, where the current follows the path of least resistance and shortest distance. Specifically, under RSW-R conditions, the annular conductive zone (ACZ) was distributed in a ring around the joint center, and the linear distance between the upper and lower electrodes' ring-shaped conductive areas was minimized, allowing current flow through the contact area between ACZ. Additionally, current also flowed through the contact area in the joint center, likely because the faying surface beneath the electrode core was tightly pressed under electrode force, reducing resistance. At 13 kA and 0.11 s under RSW-R conditions, the local current density at the joint center (near point A) exceeded that at the center of the annular-nugget (near point B), likely due to increased resistance at the annular-nugget caused by elevated temperatures, prompting the current to flow preferentially through the contact area in the joint center, where the resistance was lower. Under RSW-S conditions, although rising nugget temperature similarly caused current to flow along the outer side of the elliptical nugget, the contact area remained less than that under RSW-R conditions.

By comparing the growth of the corona bond and the nugget, it is possible to assess whether the joint has reached the conditions for expulsion. Previous studies have shown that the strength of the corona bond has a negligible effect on expulsion compared to other factors (Refs. 28, 29). Furthermore, since in-situ observation of nugget and corona bond growth rates is impossible during the experiment, this study qualitatively analyzed expulsion likelihood by characterizing the corona bond area under different electrode conditions. As shown in Fig. 14A, the region on the faying surface with a temperature between 800° and 1480°C (melting point) was defined as the plastic softening zone when the nugget diameter reached its maximum in the model. The temperature range for plastic softening was determined from the curve of 0.2% proof stress variation with temperature for DP780 steel. Figure 14B shows that, between 800° and 1480°C, the 0.2% proof stress was relatively low, and the curve tended to flatten. Figure 14C compares the experimentally obtained corona bond area with the simulated plastic softening zone

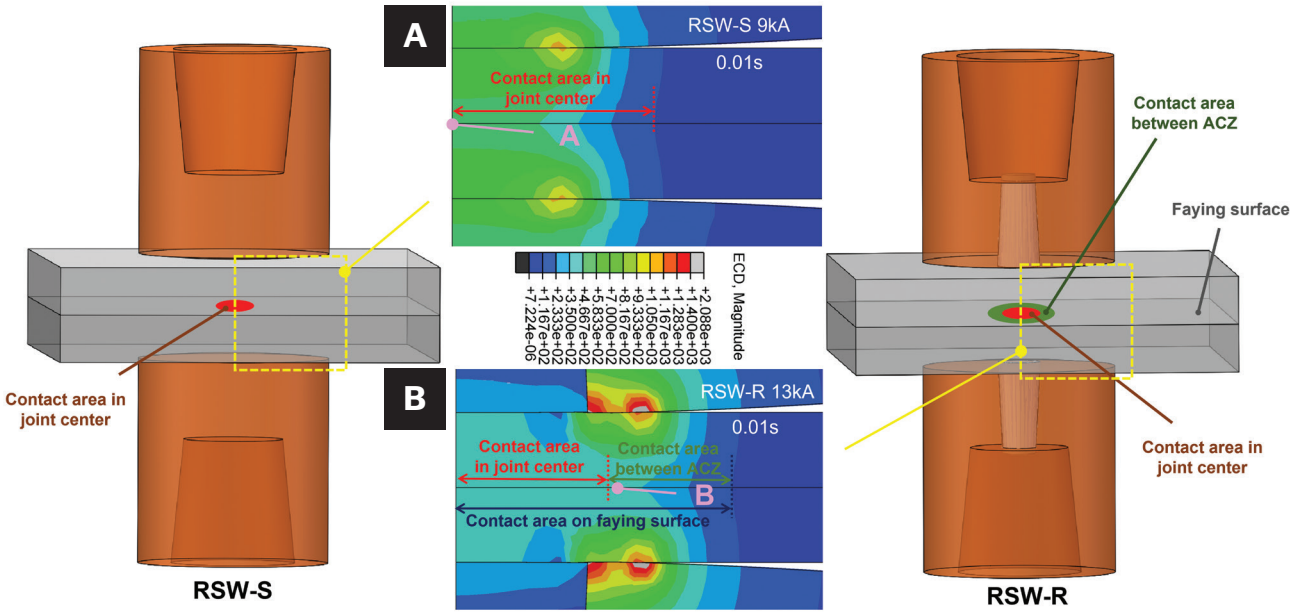

Fig. 11 — Schematic diagram of the conductive area zone of the joints by numerical simulation: A — RSW-S condition at 9kA; B — RSW-R condition at 13kA.

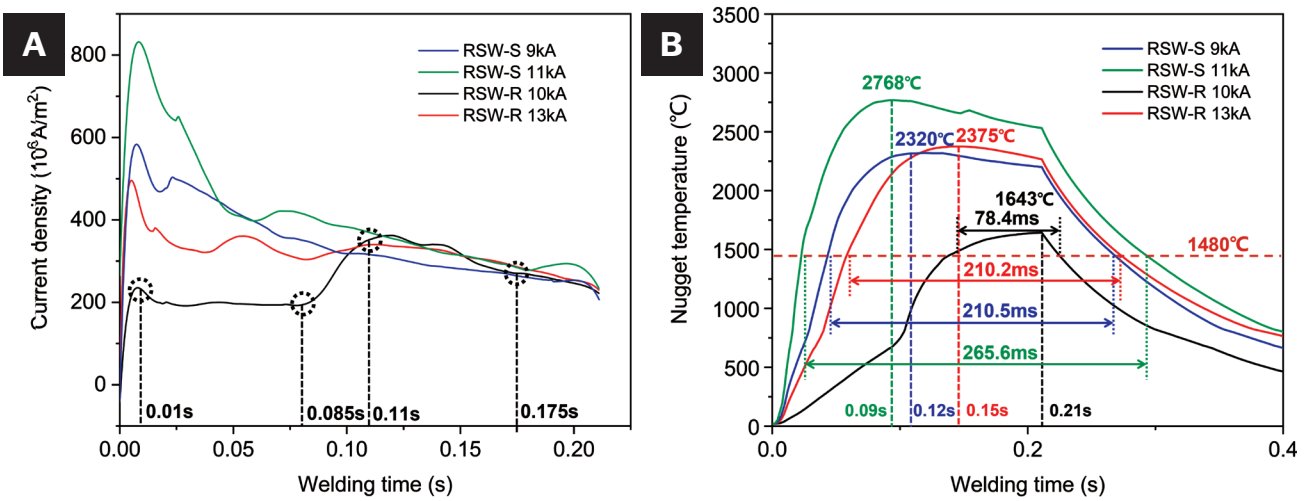

Fig. 12 — Variation of nugget temperature and current density with welding current by numerical simulation under RSW-R and RSW-S conditions: A — Current density at nugget center with welding time; B — temperature at nugget center with welding time.

area, revealing that the size of the plastic softening zone roughly corresponded to the corona bond area. Both simulation and experimental results indicated that the corona bond area decreased with increasing welding current. Within the weldability range, the corona bond area under RSW-R conditions was generally more prominent than under RSW-S conditions. This observation indicated that when the nugget diameter reached its maximum, the corona bond under RSW-R conditions more effectively suppressed expulsion, thereby expanding the weldability range compared to RSW-S conditions.

Mechanism of Annular-Nugget Growth

As shown in Figs. 6 and 7, the outer diameter of the annular-nugget was significantly more extensive than that of the elliptical nugget, regardless of the nugget diameter under the same welding parameters or the maximum diameter of nuggets before expulsion. The increase in nugget diameter was attributed to the optimized heat input mode of RSW-R, which operated in two ways. First, the position of annular-nugget growth initiation contributed to a larger diameter than elliptical nuggets. The annular high current density zone between ACZ established the initial annular

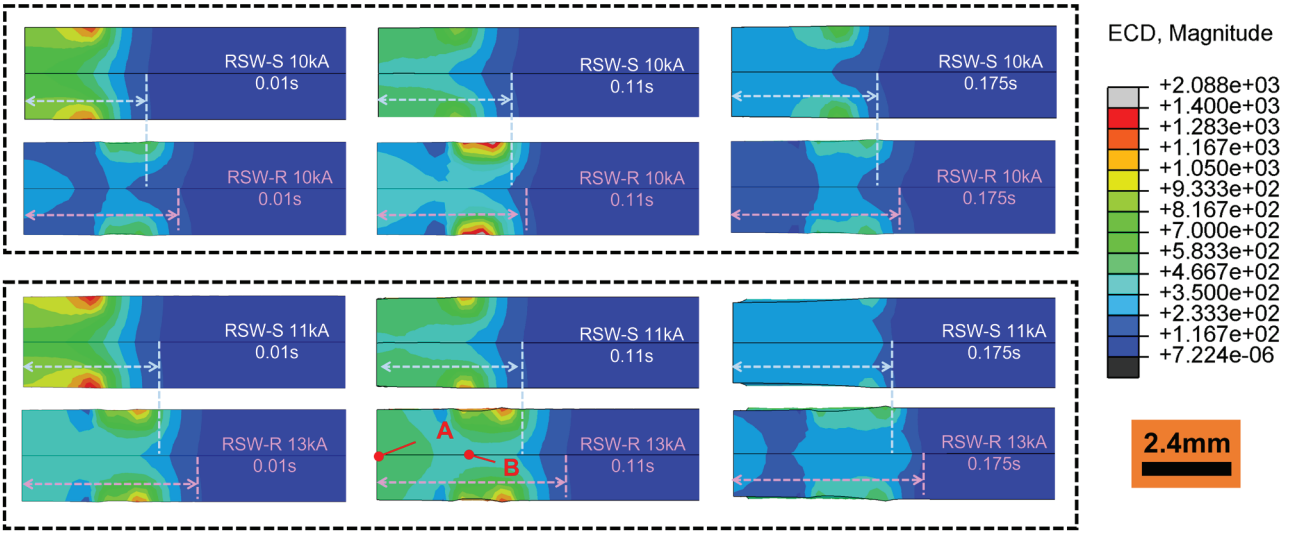

Fig. 13 — Comparison of current densities at the same welding current (10 kA) and at the maximum welding current for pullout fracture (11 kA for RSW-S, 13 kA for RSW-R) for joints by numerical simulation under two types of electrode conditions.

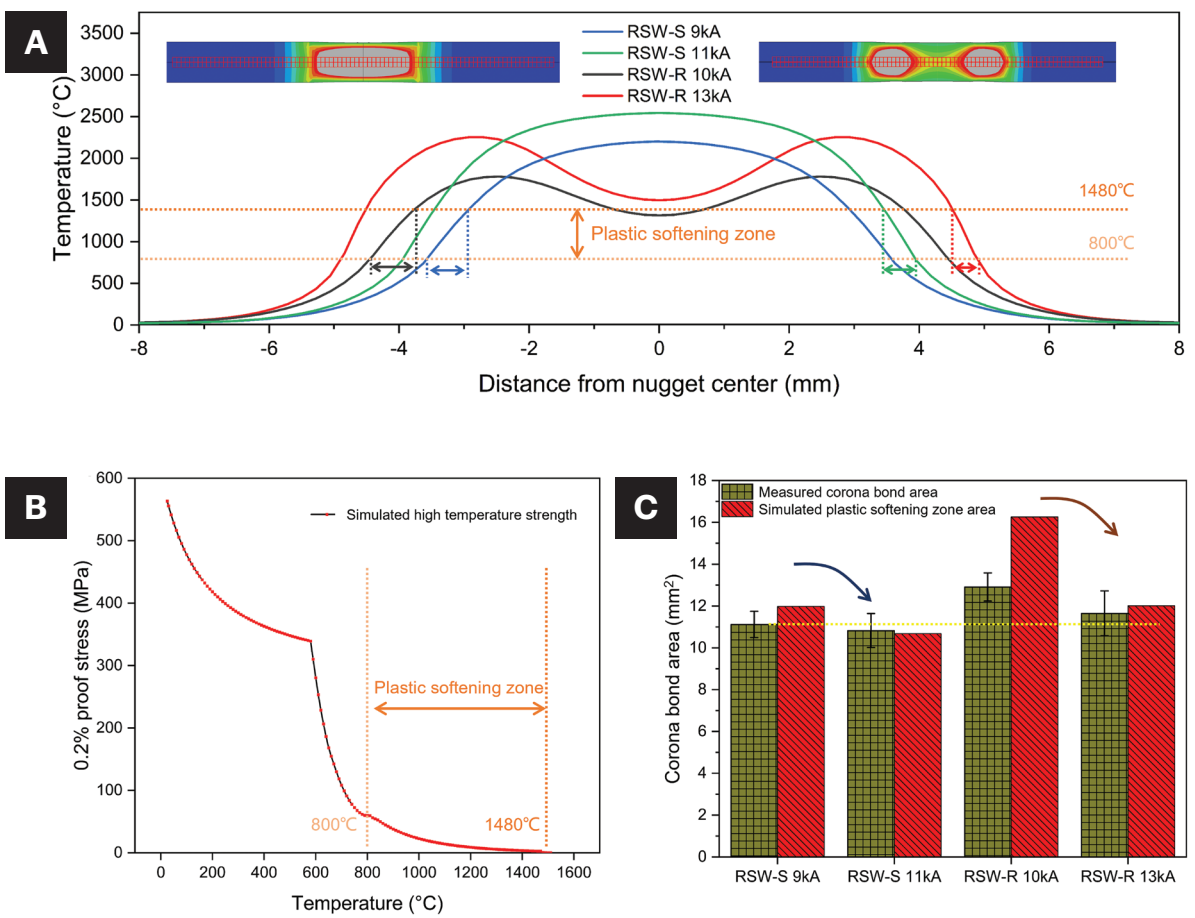

Fig. 14 — Variation of corona bond area with welding current under different electrode conditions: A — Variation of temperature with distance by numerical simulation when nugget diameter gets maximum under different electrode conditions; B — simulated high-temperature strength of DP780 steel by JMatPro; C — comparison of experimentally obtained corona bond areas with numerically simulated plastic softening zone areas.

shape of the nugget. With the influence of Joule heating, the annular-nugget grew bidirectionally, expanding inward and outward. Second, the lower current density distribution under RSW-R conditions extended the upper limit of the current range, providing favorable conditions for nugget growth.

The optimized heat input mode of RSW-R also influenced nugget penetration. The notable reduction in penetration may be attributed to the growth pattern of the annular-nugget and the lower Joule heat input. As shown in Fig. 7B, within the weldability range, the nugget area of the annular-nugget was generally more extensive than that of the elliptical nugget under RSW-S. Furthermore, as depicted in Fig. 8, the Joule heat input for the annular-nugget was lower than that for the elliptical nugget under identical welding parameters. This combination of reduced Joule heat input and increased nugget area helped limit the excessive axial growth of the nugget.

As shown in Fig. 10, the current density and temperature variations at the center of the nuggets under the RSW-R 10 kA condition differed from those under the other three parameters. During the period of 0.01–0.085 s, under RSW-R 10 kA, the sheet temperature remained low, and the faying surface maintained a large contact area due to the axial electrode force. Consequently, the current density remained low and stable throughout this period. During the period of 0.085–0.11 s, the nugget's current density under RSW-R 10 kA raised slightly, likely due to the rapid temperature increase in the nugget and a reduction in the contact area caused by the warping deformation of the sheet. After 0.11 s, the current density decreased under all four conditions as nugget growth continued, the nugget area expanded, and the nugget temperature rose.

The superior heat input method and efficient heat dissipation of RSW-R significantly reduced the indentation depth on the joint surface. Compared to RSW-S, the indentation depth at the maximum welding current was decreased by 48.65%. This improvement meets industrial requirements for surface quality in RSW joints and alleviates the stress concentrations caused by excessive indentation typical of traditional RSW methods with high heat input. Furthermore, this electrode design lowers the welding temperature, enhancing the applicability of thermally sensitive materials in RSW processes.

Conclusions

This study investigated the advantages of the new ring conductive electrode (RSW-R) over the conventional spherical electrode (RSW-S) for DP780 steel regarding weldability and nugget growth. The conclusions are as follows:

1. Under the same welding parameters, RSW-R produced larger diameter nuggets with lower Joule heat inputs than RSW-S conditions.

2. The maximum nugget diameter achieved under RSW-R was 8.24 mm, 17.38% larger than the 7.02 mm observed under RSW-S conditions. Likewise, the maximum nugget area under RSW-R was approximately 30.32% larger than that under RSW-S.

3. The surface indentation depth of joints under RSW-R was reduced by 48.65% compared to RSW-S at maximum welding currents (13 kA for RSW-R and 11 kA for RSW-S).

4. The optimized current density distribution at the faying surface under RSW-R increased the weldability range of DP780 steel by 1.5 times compared to RSW-S.

Statements and Declarations

Declaration of Competing Interest

The authors declare that they have no known competing financial interests or personal relationships that could have appeared to influence the work reported in this paper.

Acknowledgment

This work was supported by the Jilin Scientific and Technological Development Program (CN) under Grant (No.20190302044GX) and supported by the central government guided local science and technology development fund support projects (Study on Key Technologies of Intelligent Ultrasonic Imaging Detection and Evaluation of Defects in Gas Shielded Welding, 2022L3065).

References

1. Bai, X., Chen, G., Li, W., Jia, R., Xuan, L., Zhu, A., and Wang, J. 2021. Critical speeds of electric vehicles for regenerative braking. *Automotive Innovation* 4(2): 201–214.

2. Zhang, Q. K., Long, W. M., Yu, X. Q., Pei, Y. Y., and Qiao, P. X. 2015. Effects of ga addition on microstructure and properties of Sn–Ag–Cu/Cu solder joints. *Journal of Alloys and Compounds* 622: 973–978.

3. Li, Z. R., Zhang, D. P., Chen, R. M., Wang, S. L., Xia, Y. J., and Li, Y. B. 2024. Improving weldability of press hardened steel through combining stepped current pulse and magnetically assisted resistance spot welding process. *Journal of Manufacturing Science and Engineering* 146(2).

4. Ordoñez, J. H., Ambriz, R. R., García, C., Plascencia, G., and Jaramillo, D. 2019. Overloading effect on the fatigue strength in resistance spot welding joints of a DP980 steel. *International Journal of Fatigue* 121: 163–171.

5. Béal, C. T. 2012. *Mechanical behaviour of a new automotive high manganese TWIP steel in the presence of liquid zinc.* Ph.D. dissertation. Lyon National Institute of Applied Sciences.

6. Batista, M., and Brandi, S. D. 2013. Use of dynamic resistance and dynamic energy to compare two resistance spot welding equipments for automotive industry in zinc coated and uncoated sheets. *American Journal of Engineering Research* 2(6): 79–93.

7. Bhattacharya, D. 2018. Liquid metal embrittlement during resistance spot welding of Zn-coated high-strength steels. *Materials Science and Technology* 34(15): 1809–1829.

8. Kong, J. P., and Kang, C. Y. 2016. Effect of alloying elements on expulsion in electric resistance spot welding of advanced high strength steels. *Science and Technology of Welding and Joining* 21(1): 32–42.

9. Sun, X., Stephens, E. V., and Khaleel, M. A. 2008. Effects of fusion zone size and failure mode on peak load and energy absorption of advanced high strength steel spot welds under lap shear loading conditions. *Engineering Failure Analysis* 15(4): 356–367.

10. Ling, Z., Chen, T., Kong, L., and Wang, M. 2022. Effects of cover sheets on the nugget growth and fracture behavior of resistance

spot welded Q&P980 steel joints. *Chinese Journal of Mechanical Engineering* 35(1).

11. Gerardo, M-S., Antonio, C., Jesús, D-G. 2021. Influence of the process parameters on the quality and efficiency of the resistance spot welding process of advanced high-strength complex-phase steels. *Metals* 11(10).

12. Díaz, C. A., Martínez, E. E., Saldana, R., and Gutiérrez-Castaneda, E. J. 2024. Development of Q&P steels of third generation under conditions simulating a continuous annealing process, and evaluation of their weldability by the RSW process. *Materials Letters* 365.

13. Xu, H. L., and Fang, X. F. 2024. A new resistance insert spot welding method for injection molded FRP–steel component. *The International Journal of Advanced Manufacturing Technology* 132: 2017–2043.

14. Chen, T., Ling, Z., Wang, M., and Kong, L. 2020. Effect of a slightly concave electrode on resistance spot welding of Q&P1180 steel. *Journal of Materials Processing Technology* 285: 116797.

15. Watanabe, G., Amago, T., Ishii, Y., Takao, H., Yasui, T., and Fukumoto, M. 2016. Improvement of cross-tension strength using concave electrode in resistance spot welding of high-strength steel sheets. *AIP Conference Proceedings* 1709.

16. Ren, D., Zhao, D., Li, C., Liu, L., and Zhao, K. 2019. Resistance ceramic-filled annular welding of thin steel sheets. *Journal of Manufacturing Processes* 45: 588–594.

17. Zhao, D., Ren, D., Song, G., Zhao, K., Liu L., and Zhang, Z. 2020. Comparison of mechanical properties and the nugget formation of composite ceramic-centered annular welding and traditional resistance spot welding. *International Journal of Mechanical Sciences* 187: 105933.

18. Ren, D., Zhao, D., Zhao, K., Liu, L., and He, Z. 2019. Resistance ceramic-filled annular welding of DP980 high-strength steel. *Materials & Design* 183: 108118.

19. AWS C1.1M/C1.1:2012. *Recommended Practices for Resistance Welding*. American Welding Society (AWS) C1 Committee on Resistance Welding.

20. Resistance Welding Manufacturing Alliance (RWMA). 2023. *Resistance welding manual* (Revised 4th edition). American Welding Society (AWS).

21. Xia, Y. J., Lv, T. L., Ghassemi-Armaki, H., Li, Y. B., and Carlson, B. E. 2023. Quantitative interpretation of dynamic resistance signal in resistance spot welding. *Welding Journal* 102(4): 69–87.

22. AWS D8.9M:2022. *Test methods for evaluating the resistance spot welding behavior of automotive sheet steel materials*.

23. Mahmud, K., Murugan, S. P., Cho, Y., Ji, C., Nam, D., and Park, Y. D. 2021. Geometrical degradation of electrode and liquid metal embrittlement cracking in resistance spot welding. *Journal of Manufacturing Processes* 61: 334–348.

24. Lu, Y., Peer, A., Abke, T., Kimchi, M., and Zhang, W. 2018. Subcritical heat affected zone softening in hot-stamped boron steel during resistance spot welding. *Materials & Design* 155: 170–184.

25. Wang, S., Xu, G., Dong, J., Zheng, G., and Gu, X. 2023. Research on shape control and performance of joint nugget during RSW processing. *The International Journal of Advanced Manufacturing Technology* 128(3–4): 1169–1178.

26. Prigogine, I., Defay, R., and Everett, D. H. 1954. *Chemical Thermodynamics* 32, London.

27. Shen, Y., Xia, Y. J., Li, H., Zhou, L., Li, Y. B., and Pan, H. T. 2021. A novel expulsion control strategy with abnormal condition adaptability for resistance spot welding. *Journal of Manufacturing Science and Engineering* 143(11): 111009.

28. Valaee-Tale, M., Sheikhi, M., Mazaheri, Y., Ghaini, F. M., and Usefifar, G. R. 2020. Criterion for predicting expulsion in resistance spot welding of steel sheets. *Journal of Materials Processing Technology* 25: 116329.

29. Zhang, H., and Senkara, J. 2011. *Resistance welding: Fundamentals and applications*. Leiden, Netherlands: CRC Press.

SHENGWEI WANG, **GUOCHENG XU**, **JUAN DONG**, **YU QIU**, and **XIAOPENG GU** (*guxp@jlu.edu.cn*) are with Key Laboratory of Automobile Materials of Ministry of Education, School of Materials Science and Engineering, Jilin University, Jilin, China. **QIUYUE FAN** is with Fujian Provincial Key Laboratory of Welding Quality Intelligent Evaluation, Longyan University, Longyan, China. **ZHIYI HUANG** is with CRRC Changchun Rail Transit Co., Ltd, Changchun, China.